

Investigation of Strain-Rate Effects in Ni/PU Hybrid Foams under Low-Impact Velocities

Markus Felten, Michael Fries, Andy Pullen, William G. Proud, and Anne Jung*

Metal foams are often used as energy absorbers and lightweight materials. Inspired by a natural blueprint, open-cell metal foams can significantly reduce the mass of a structure. The innovative manufacturing process of electrodeposition provides the possibility to customize the coating layer thickness of nickel (Ni) on a polyurethane (PU) precursor foam. Consequently, the mechanical properties can be adjusted according to the requirements of the expected application. Herein, quasistatic compression tests and low-velocity impact tests are conducted on open-cell Ni/PU hybrid foams to investigate the strain-rate effects for strain rates in the range of 10^{-3} to 550 s^{-1} . Furthermore, digital image correlation is performed with the intention of comparing the micromechanical deformation mechanisms under quasistatic loading with those under dynamic loading. For the first time, the heat evolution at different impact velocities of metal foams has been investigated with an infrared camera.

structural material.^[5] Furthermore, metal foams exhibit the capability to absorb high amounts of kinetic energy at an almost constant stress level in compression. Consequently, metal foams can be used as energy absorbers for crash elements in different industrial sectors such as aerospace, packaging, and the defense industry.^[8,9]

To phenomenologically describe the material properties, it is beneficial to distinguish three different hierarchical scales. The length of the macroscale comprises the whole size of the specimen. The mesoscale covers the length of several pores and the microscale includes the length of single struts. The stress–strain curve in compression can be divided into three phases. Within the first phase, which is called pseudoelastic, the struts deform under bending

1. Introduction

Although the origin of metal foams dates back to the 1950s, this class of material has gained considerable attention during the last few decades.^[1] A range of different materials, new manufacturing processes, and optimized pore structures have been developed recently.^[2–6] Metal foams are cellular materials mimicking the structure of femur bone or wood.^[7] This cellular design concept combines lightweight construction through material savings with a high specific stiffness. This inherent material property leads to their application as a lightweight

almost elastically. Nevertheless, yielding emerges in a few struts so that the material behavior is not exclusively elastic.^[10] When the compressive strength, which is termed the plastic collapse stress (PCS), is reached, a whole pore layer collapses and the stress–strain curve achieves the second phase with a distinct plastic stress plateau. As a result of the successive collapse of further pore layers on the mesoscale, the stress plateau emerges over a wide range of strain with a more or less pronounced increase in stress. Localized deformation bands are generated.^[11] The third phase arises after all the pore layers have been collapsed and the stress increases due to rising densification and contact between the struts.^[6] As a result of the only slightly increasing plateau stress and hence the energy absorption on a nearly constant stress level, metal foams are highly suitable for energy absorption applications. They are used in crumple zones for cars, trains, and in the packaging industry. Further potential applications for military and civil structures in terms of protection against ballistic impacts found in the literature are space debris shields, claddings, armor systems, and helmets.^[12–15]

Metal foams consist of a variety of materials. Aside from uniform materials such as Al, Ni, Ti, Cu, Mg, or steel, there are innovative approaches such as metal matrix composites (MMC), which show the transformation-induced plasticity (TRIP) effect or metal matrices strengthened with ceramic cenospheres.^[6,16,17] To improve the mechanical properties of uniform material foams such as Al, open-cell metal foams have been coated with Ni via electrodeposition.^[18,19] Coating polyurethane (PU) precursor foams with Ni offers another approach to produce hybrid metal foams.^[20] The main advantage of these foams is the lower production cost. The mechanical properties can be adjusted

M. Felten, M. Fries, Dr. A. Jung
Institute of Applied Mechanics
Saarland University
Campus A4.2, 66123 Saarbrücken, Germany
E-mail: anne.jung@mx.uni-saarland.de

A. Pullen
Department of Civil and Environmental Engineering
Imperial College London
London SW7 2AZ, UK

Dr. W. G. Proud
Institute of Shock Physics, Blackett Laboratory
Imperial College London
London SW7 2AZ, UK

 The ORCID identification number(s) for the author(s) of this article can be found under <https://doi.org/10.1002/adem.201901589>.

© 2020 The Authors. Published by WILEY-VCH Verlag GmbH & Co. KGaA, Weinheim. This is an open access article under the terms of the Creative Commons Attribution License, which permits use, distribution and reproduction in any medium, provided the original work is properly cited.

DOI: 10.1002/adem.201901589

precisely by varying the thickness of the coating, depending on the intended application.

This class of open-cell metal foams consists of 3D connected and stochastically distributed pores. Such a cellular construction reduces the weight to a minimum and allows liquids to flow through the foam. This capability expands the range of potential applications. Open-cell metal foams are used as heat exchangers, filters, silencers, and vibration dampers.^[21–24] The foam must be able to withstand partially static as well as dynamic loads in the different applications.

According to Deshpande and Fleck^[25] and Zhao et al.,^[14] there are four reasons that cause strain-rate effects in cellular materials. The first reason affects closed-cell foams or fluid-filled open-cell foams. The pressure within the pores rises caused by the retarded movement of the fluid compared with the deformation of the framework. The second reason for strain-rate sensitivity correlates with a shock wave propagation and enhancement at velocities of above 50 m s^{-1} . This effect can be neglected for low velocity impacts. In accordance with the mechanistic model developed by Gibson and Ashby,^[26] the material properties of cellular materials can be expressed by the correlated properties of the strut material. Thus, the third reason for strain-rate sensitivity in cellular materials is connected to strain-rate effects in the strut material. The fourth reason is induced by the structural response of the mesostructural framework. These microinertia effects lead to a change in the deformation mode.^[27–29] However, there is a bending-dominated deformation mechanism under quasistatic loads the mode changes to a distinct stretching as a result of delayed buckling of the struts under dynamic loads.^[27–29]

The mechanical behavior under quasistatic loads has been the primary focus in the literature despite the significant relevance of strain-rate sensitivity. Most of the dynamic testing on cellular materials has been conducted with a split Hopkinson pressure bar (SHPB).^[14,30,31] This technique comprises high strain rates from 10^3 to 10^4 s^{-1} . There are only a few investigations of moderate strain rates between 10^1 to 10^3 s^{-1} as they occur in the automotive sector. The most widespread methods to investigate moderate strain rates on metal foams are the dynamic application of a universal testing machine, the pendulum impact method, a gas gun, or the drop-weight tower.^[32–38] Drop-weight tests are either conducted with a hemispherical tip as an indentation test or with a flat tip for compression tests.^[11,30,39–47] Drop-weight tests have several advantages. The method exhibits good repeatability and simple implementation as well as easy control. A drop weight of mass m is lifted to a predetermined height h above the specimen. Under the acceleration of gravity g , the drop weight has the potential energy $E_{\text{pot}} = mgh$. When the drop weight is released, potential energy becomes kinetic energy $E_{\text{kin}} = 0.5mv^2$. At the moment of impact, the kinetic energy is equal to the predetermined potential energy. As a result, the impact velocity v_0 is expressed by

$$v_0 = \sqrt{2gh} \quad (1)$$

Therefore, the impact velocity and the initial strain rate are independent of the mass. The latter decreases during the impact due to the energy absorbed by the specimen, the force required for this decelerates the mass. In contrast to this, the strain rate during a quasistatic compression test is typically almost constant.

For experiments in which specimens are directly impacted, and where the impact force is measured by the test rig, the stress–strain curve can be derived from the force-time history recorded during the experiment. First, the acceleration-time history $a(t)$ is calculated according to

$$a(t) = \frac{F(t)}{m} \quad (2)$$

In the next step, the displacement-time history $u(t)$ is calculated via a double integration

$$u(t) = \int (v_0 - \int a(t)dt)dt \quad (3)$$

The absorbed energy $E(t)$ is finally determined by

$$E(t) = \int F(u)du \quad (4)$$

Two assumptions were connected with this calculation. 1) The tip of the drop weight and the framework underneath the specimen are considered as ideal rigid, so that the whole energy is absorbed by the specimen. 2) A perfect contact between the head of the drop weight and the specimen is assumed. Therefore, any range of surface roughness is neglected.

Sandwich materials including aluminum honeycomb foam structures were investigated by Chen et al.^[47] with a flat tip of a drop-weight test. Mines et al.^[48] compared the mechanical behavior of microlattices made of a titanium alloy and stainless steel manufactured by selective laser melting with conventional aluminum honeycombs under drop-weight tests. A series of different syntactic foams varying in proportion and size of the ceramic particles were tested by Altenaiji et al.^[30,46] at several moderate strain rates. The experimental investigation of the mechanical behavior of metal foams under drop-weight impact tests focused predominantly on closed-cell aluminum foams.^[43–45] Jung et al.^[11] investigated the effect of strain rate on the compression of open-cell aluminum foams and Ni/Al hybrid composite foams from quasistatic to low-velocity impact loading. Only a few of these mechanical investigations were extended by a digital image correlation (DIC) using a high-speed camera or the analysis of impact damage areas using thermographic images.^[11,39,49]

In this study, the effect of strain rate on the compressive stress/strain behavior of open-cell Ni/PU hybrid composite metal foams was investigated. Strain rates ranged from quasistatic (10^{-3} s^{-1}) by servohydraulic loading to low-velocity impact (550 s^{-1}) using a drop-weight impact rig. The micromechanical deformation mechanism was further analyzed using DIC. Several tests were recorded with an infrared (IR) camera to observe the heat evolution at different impact velocities.

2. Experimental Section

2.1. Specimen Preparation

The template structure for the Ni/PU hybrid foams is a PU foam (Schaumstoff Direkt Rüdiger Nolte, Enger, Germany) with an approximate pore size of 20 ppi (pores per inch) and an average density of 0.022 g cm^{-3} . The specimens were cut to a cylindrical

shape of either 30 or 50 mm diameter and a height of 20 mm by means of hot-wire cutting. To gain electric conductivity for the PU foams, the specimens were coated with Graphit 33, a conductive varnish by CRC Kontakt Chemie, Iffezheim, Germany. The conductive layer was applied by a dip coating process (Figure 1d). The carbon-coated PU foam was penetrated by a copper wire at four different points to connect the specimens to the power supply. In the process of electrodeposition, the carbon-coated foam was the cathode and was placed in the center of a double-walled hollow cube. The walls of the cube consist of expanded titanium metal and are filled with S-depolarized nickel balls by A.M.P.E.R.E. GmbH, Dietzenbach, Germany, which will be dissolved as a sacrificial anode during the electrochemical deposition process. This special setup was required because of the complex 3D pore geometry of the foam. A commercial nickel sulfamate electrolyte (Enthone GmbH,

Table 1. Mean density, quantity, and standard deviation per specimen size.

Ø specimen [mm]	Quantity	Density [g cm ⁻³]
30	21	1.191 ± 0.222
50	14	0.943 ± 0.101

Langenfeld, Germany) with 110 g L⁻¹ nickel was used at 50 °C and a pH of 3.5. The deposition was conducted at an average current density of ≈1.4 mA cm⁻² to realize a nanocrystalline average grain size of the nickel coating. The determined average thickness of the nickel coating was 150 µm. The whole preparation method is shown in Figure 1. As foams generally do not have a perfectly homogeneous microstructure, the surface area in commercial PU foams varied by 10–15%. Because computer tomography cannot be performed for every individual specimen to be coated to adjust the exact surface for every specimen, the current density varied slightly for the same applied current leading to some variations in the density of the hybrid foam specimens. The average density of all produced Ni/PU hybrid foams is shown in Table 1.

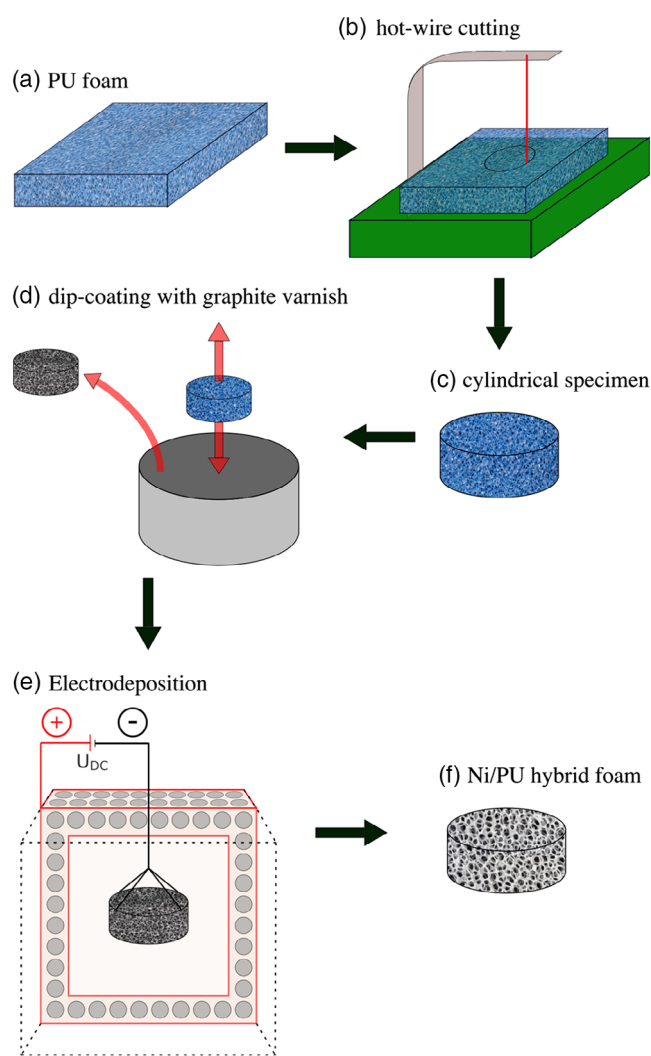


Figure 1. Preparation process of a Ni/PU foam: a) foam sheet as delivered, b) hot wire cutting process, c) cylindrical specimen, d) dip-coating process with conductive graphite varnish, e) electrodeposition: specimen placed in the center of a double walled hollow cube surrounded by Ni pellets and connected to a DC power supply (section without front wall), f) Ni/PU hybrid foam.

2.2. Quasistatic Compression Tests

The quasistatic compression tests were conducted with a Shimadzu servohydraulic testing machine with a maximum load of 50 kN. All specimens were studied at a strain rate of 10⁻³ s⁻¹ under displacement control.

2.3. Drop-Weight Tests

The drop-weight tests were performed with an Instron Dynatup 9250HV drop-weight tower (see schematic representation in Figure 2a). The maximum drop height of 1250 mm indicates an impact velocity of 5 m s⁻¹. The drop tower was equipped with an acceleration spring system, which provided an additional 600 J and enables impact velocities up to 20 m s⁻¹ for low drop-weight masses. The system allowed an ultimate simulated drop height of 20 m and a maximum impact energy of 1603 J. The drop weight consists of a flat impact head, an integrated load cell, which is recorded by a 12 bit analog-to-digital converter at up to 1.17 Hz for 7 ms, above the tip and a variable impact mass. The specimens were placed directly underneath the drop weight on a rigid support block. The impact buffers decelerated the drop weight after deforming the specimens to a certain strain and prevented the drop weight from hitting the specimens more than once. The impact velocities were measured with light gates just before the drop weight hits the specimen.

The impact mass was varied between 6.8 and 84.5 kg at different drop heights to achieve nearly constant impact energies of 1000 J while executing different impact velocities. The impact force was measured with a load cell integrated into the drop weight, just above the impact head. This load cell records the force history decelerating the mass above its sensing element, rather than that acting on the entire drop-weight mass, so it was necessary to apply a correction to obtain the force history

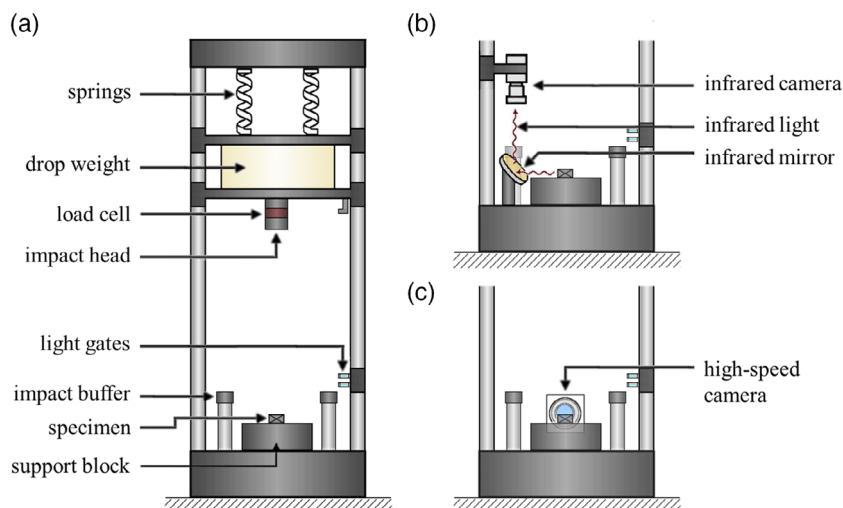


Figure 2. Schematic representation of the experimental arrangement: a) entire drop-weight tower, b) setup for the IR camera, and c) the high-speed camera.

at the impact interface. The complete drop-weight mass m_{DW} consists of the mass above the sensing element m_1 , plus the mass of the impact head m_2 between the sensing element and the impact interface, $m_{DW} = m_1 + m_2$. The measured force-time history $F_1(t)$ was corrected to obtain the force-time history $F_2(t)$ applied on the specimen by considering the entire drop weight as a rigid body, experiencing the same acceleration according to

$$\frac{F_1}{m_1} = \frac{F_2}{m_1 + m_2} \Rightarrow F_2(t) = \frac{m_{DW}}{m_{DW} - m_2} F_1(t) \quad (5)$$

A double integration of the corrected force-time history (see Equation (3) and (5)) was conducted to obtain the stress–strain diagrams of the drop-weight tests.

The experiments were recorded with a Vision Research Phantom V611 high-speed camera (Figure 2c). The V611 achieves a maximum frame rate of 6242 frames per second (fps) at a full resolution of 1280×800 . The frame rate can be increased up to 1 000 000 fps by reducing the resolution. A frame rate of 17 000 fps with a resolution of 800×400 was used in this study.

Several experiments were observed with a Flir A600 Series IR camera. The plexiglass safety enclosure of the impact rig is transparent to visible light but opaque to infrared, so the IR camera had to be placed within the impact chamber. The IR camera was positioned vertically due to a lack of space within the impact chamber (Figure 2b). A 50 mm diameter broadband IR laser mirror from Edmund Optics Ltd was arranged at an angle of 45° , to appropriately reflect the image of the specimen to the camera (Figure 2b).

3. Results and Discussion

3.1. Stress–Strain Behavior and Energy Absorption Capacity

Figure 3 shows representative stress–strain curves of Ni/PU hybrid foams under quasistatic (blue) and dynamic (black) loading. After PCS, the quasistatic stress rises and falls due to the

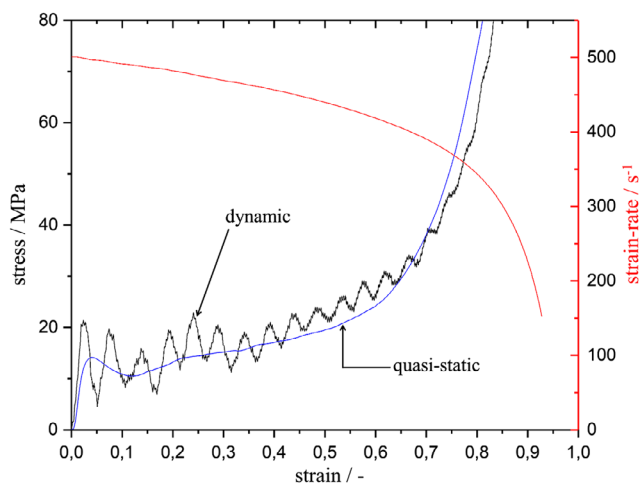


Figure 3. Comparison of representative stress–strain curves for Ni/PU hybrid foams under quasistatic and dynamic loading. The right y -axis indicates the reduction in strain rate during the dynamic impact test.

successive collapse of pore layers on the mesoscale. The dynamic stress–strain data indicate a superimposed oscillation which originates from vibrations of the test rig. According to Juntikka and Hallström,^[50] these vibrations are correlated with the eigenfrequency of the load cell. The eigenfrequency varies with the modification of the drop weight and subsequently the amplitude of the oscillations. Furthermore, Figure 3 shows a reduction in strain rate during the impact test (red). The kinetic energy of the free falling mass is progressively absorbed by the specimen, reducing its velocity and therefore the strain rate. Consequently, the experiments represent the boundary conditions of a real impact, where the strain rate is also reduced. Both the dynamic and the quasistatic stress–strain diagrams exhibit a pronounced hardening in the plateau phase. Such macroscopic strain hardening in foams is influenced on the one hand by strain hardening of the strut material on the microscale and on the other hand

by geometric strain hardening based on a strut reorientation of the mesoscale.^[51] Kolluri et al.^[52] indicated a correlation between an increase in density and an enhanced strain hardening. Jung et al.^[11] noted that the deviation from an ideal plastic deformation might be also related to an inhomogeneity in the coating thickness. Due to shielding effects and limited mass flow during the deposition process, a homogenous Ni layer thickness cannot be achieved over the entire specimen. According to Jung et al.,^[11] the coating thickness in the top and bottom zones of the specimens is larger than that in the middle part. When the compressive strength is reached, the weakest pore layer in the middle of the Ni/PU foam collapses. As an effect of the mass transport limitation, the coating thickness increases subsequently from pore layers in the middle of the foam to the outer parts resulting in the observed geometric hardening in the macroscopic stress–strain curves.^[10,53] The PCS and the energy absorption capacity up to 0.6 strain will be the considered benchmarks to evaluate the strain-rate sensitivity of Ni/PU hybrid foams. The PCS is an essential benchmark as it indicates the transfer from a pseudoelastic to a plastic material behavior. A variation of the PCS as a function of strain rate would affect the design of a lightweight component. Moreover, in terms of an application as an energy absorber, the absorbed energy outlines a useful reference point. An altered capability of energy absorption could change the effectiveness of the material and would certainly complicate the design of a component, at the same time. The Ni/PU foams show a pronounced scattering in density. Therefore, it is necessary to examine the dependence of density more closely, to distinguish effects caused by the influence of scattering in density from potential strain-rate effects. The PCS was determined as the first stress peak in the stress–strain curves. **Figure 4a** shows the PCS as a function of density. The PCS for both specimen diameters approximately linearly increases with density. This is the case for the quasistatic and the dynamic experiments. There seems to be no effect of the specimen diameter on the PCS; however, the PCS determined from the dynamic tests is about 5 MPa higher than for the quasistatic loadings. Due to the superposition of the material-related stress–strain curve with the oscillations caused by the

eigenfrequency of the test rig, errors can occur while using the first stress peak as a PCS. However, up to a strain rate of 250 s^{-1} , additional oscillations caused by the eigenfrequency of the utilized test rig can be completely excluded during evaluation. Thus, the increase in PCS for strain rates up to 250 s^{-1} is purely a material- or structure-related strain rate effect. With increasing drop weight and thus increasing strain rate, the oscillations due to test rig vibration increase. However, as the real PCS sometimes coincides with a wave crest and sometimes with a wave trough from the eigenfrequency-induced oscillations, averaging leads to reliable results.

Figure 4b shows the energy absorption capacity also called strain energy density, which is equal to the area underneath the stress–strain curves as function of density. Similar to the PCS, the energy absorption capacity increases linearly with density. In contrast to the PCS, there is no pronounced difference between quasistatic and dynamic experiments. Due to the linear dependency of both benchmarks, PCS and energy absorption capacity, for the purposes of comparative analysis, it is useful to consider the PCS and energy absorption capacity per unit density.

Figure 5a shows the PCS values normalized with respect to density against strain rate for both specimen types. The normalized quasistatic PCS is around 15 MPa cm g^{-1} for both specimen types considering the error bars in **Figure 5a**. The normalized dynamic PCS is around 25 MPa cm g^{-1} for both specimen types independently of the strain rate. Nevertheless, the dynamically determined PCS is two-thirds higher than the quasistatically determined PCS and thus shows a clear strain-rate dependency for the PCS. **Figure 5b** shows the energy absorption capacity with respect to density up to 0.6 strain for both specimen types under quasistatic and dynamic loading as function of strain rate. Considering the error bars, there is no strain-rate effect for the energy absorption capacity regardless of the specimen size. Independently of specimen size and strain rate, the energy absorption capacity per density is about $10 \text{ MPa cm}^3 \text{ g}^{-1}$.

The pronounced strain-rate effect of the PCS for both specimen diameters is a result of microinertia effects arising

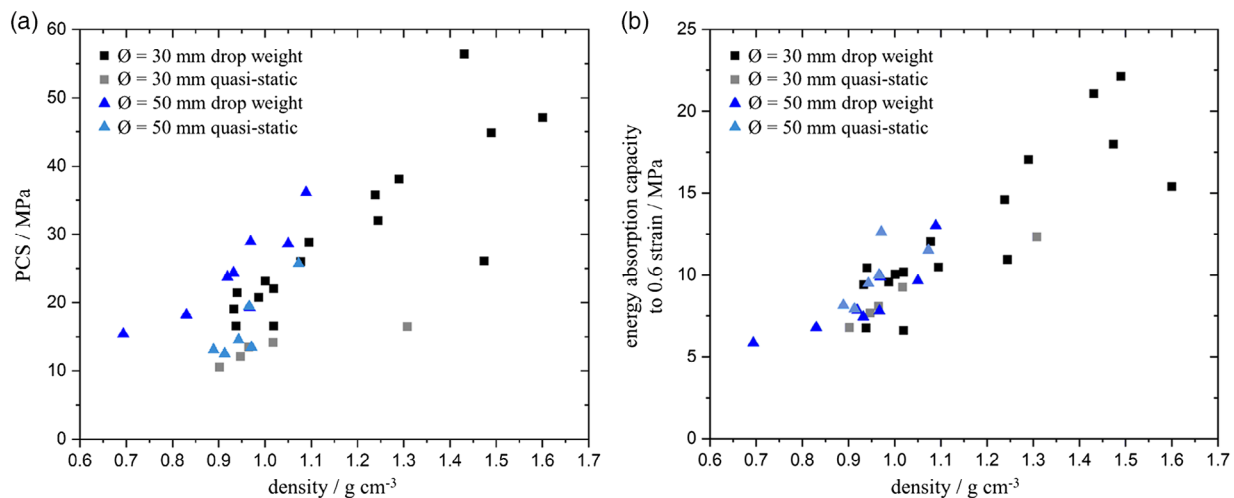


Figure 4. a) PCS and b) energy absorption capacity as a function of density for the 30 and 50 mm Ni/PU hybrid foams under quasistatic and dynamic compression.

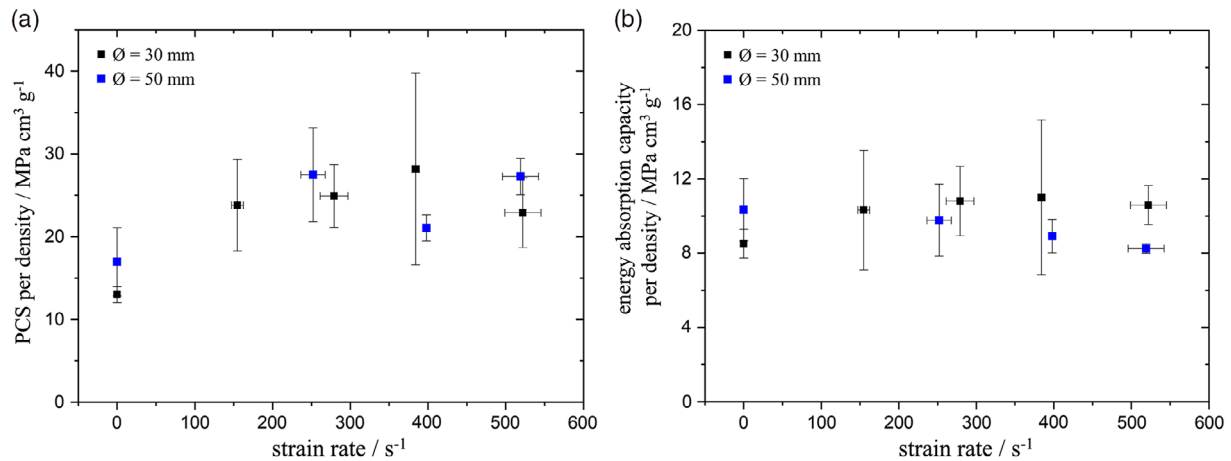


Figure 5. a) PCS and b) energy absorption capacity up to 0.6 strain normalized with respect to density as a function of strain rate for the 30 and 50 mm Ni/PU hybrid foams under quasistatic and dynamic compression.

during the deformation according to Calladine and English^[29] leading to a change in the mesoscopic deformation mechanism under quasistatic and dynamic loading. Because there is no effect on the energy absorption capacity, the strain-rate sensitivity of nickel can be neglected for the entire foam. Therefore, the nickel coating has no significant influence on the homogenized strain-rate-dependent material behavior of the Ni/PU hybrid foams. The negligible effect of specimen diameter at constant specimen height and hence equal number of pores in loading direction on the energy absorption capacity shows that the changes in the lateral dimensions have no effect on the energy absorption capacity.

3.2. Influence of Evolving Specimen Temperature during Impact on the Mechanical Behavior

Impact experiments typically have a duration of just a few milliseconds and significant transfer of thermal energy to the surrounding environment is not possible, so such tests can often be considered adiabatic. In contrast, very low-rate experiments can be considered as isothermal and temperature rises due to plastic straining rapidly dissipate to the environment. Consequently, an investigation of the temperature evolution within the specimen during impact is indicated, as thermal softening (strength reduction at elevated temperature) may obscure potential strain-rate hardening (strength increase). **Figure 6** shows a representative sequence of images from an impact test on a 30 mm specimen, observed with an IR camera. Figure 6a shows the thermal state before the impact. The specimen is

approximately in thermal equilibrium, both internally and with respect to its surroundings, so the Ni/PU hybrid foam cannot be clearly distinguished from the environment at this stage. The temperature of the specimen increases during the impact (Figure 6b,c) and the temperature difference to the environment rises, so that the shape of the specimen becomes distinctly visible. Figure 6d shows the condition immediately after the impact. At this stage, the IR camera is indicating the maximum temperature of the specimen. The images show that the specimen does not heat up uniformly over the entire observed IR image. The maximum temperatures were recorded inside the specimen, whereas individual struts at the edge have a significantly lower temperature. In general, the drop-weight tests are quasiadiabatic tests. The deformation of the individual struts causes a temperature increase in the foam. The struts at the edge of the specimen have fewer connections than struts inside the foam. Because the edge struts only have one connection to the rest of the foam structure, the deformation of the struts in the edge area and thus temperature increases are much lower than in the inner foam. Despite the fact that the test is quasiadiabatic in global terms, dissipation effects occur at the edges as a kind of size effect similar to the mechanical size effect in foams. The smaller cross-section of individual struts and very thin nature of the Ni coating will have allowed thermal energy to dissipate relatively quickly to the surroundings. Thermal energy transport from within the specimen has a longer path, so is slower. In general, local temperature fields received from IR thermography measurements can be compared with fields deduced from DIC analysis to get a deeper insight in the mesomechanical deformation mechanism.^[11,39,49]

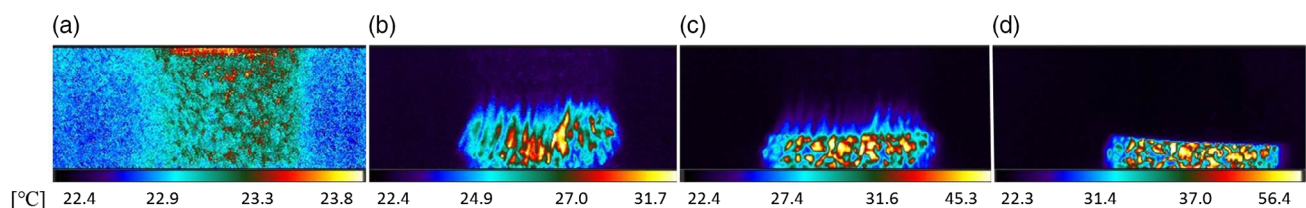


Figure 6. IR images of the heat evolution during a drop-weight test conducted at a strain rate of 150 s⁻¹ on a 30 mm Ni/PU hybrid foam.

However, this analysis has been restricted by the relatively low frame rate of the used IR camera, which allowed only two to three images during the drop-weight experiments. As a result, a direct correlation of local temperature fields and strain fields was not possible in this study. Using a high-speed IR camera, it would be possible to study the evolution of the deformation bands and compare the temperatures with the local strains determined by DIC.

In Figure 6, the maximum temperature of the specimen is in a range of 30 to 56 °C after the impact, across the entire specimen. Figure 7 shows the maximum observed temperature

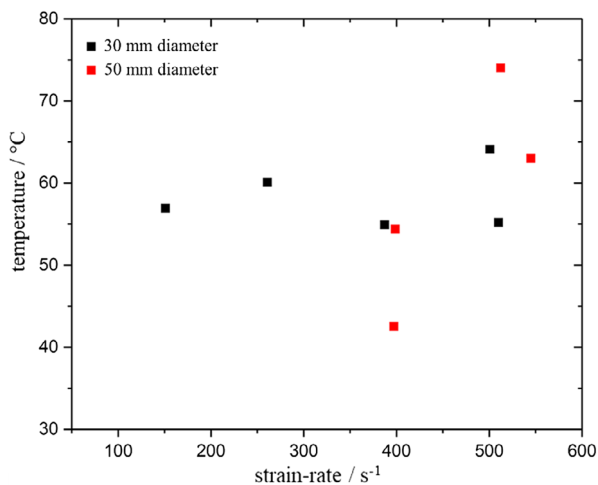


Figure 7. Determined maximum temperature recorded with an IR camera for the 30 and 50 mm Ni/PU hybrid foams under dynamic loading as function of strain rate.

against strain rate. The diagram shows a constant maximum temperature of about 60 °C for the examined Ni/PU hybrid foams with a diameter of 30 mm. However, the temperature increases with higher strain rates for the 50 mm Ni/PU hybrid foams, from an average temperature of 50 up to 70 °C with a strain rate of 400 and 550 s⁻¹, respectively. The variation in the temperature development for the same material is the consequence of different specimen geometries. The heat situation of the specimen during the drop-weight tests must not only be considered 1D, but the lateral heat transport to the free edges must also be considered. The larger volume in the specimens with 50 mm diameter generates more heat than in the specimens with 30 mm diameter. A possible heat transport in longitudinal direction from the metallic support block via the specimen to the impact head does not result in differences for the two specimen sets. Due to the lower heat generation during deformation in the edge areas of the specimen, the edges are cooler than the rest of the specimen so that a lateral heat transport from the ridges inside the specimen to the edge ridges occurs. In the specimens with a diameter of 50 mm the edge area is further away from the hot center of the foam than in the specimens with a diameter of 30 mm. Therefore, the temperature in the 50 mm specimens is higher than in the 30 mm specimens. The heat transport during the quasistatic tests was relatively fast, compared with the deformation, so that the specimens remained approximately in equilibrium with the environment and can be considered to have been constant temperature. For this reason, these results are not shown in Figure 7. Because the evolving temperature of the 30 mm in diameter specimens is constant over the entire strain-rate range, the temperature influence on the mechanical material behavior also remains the same. According to this, strain-rate-dependent behavior would be equally weakened, but

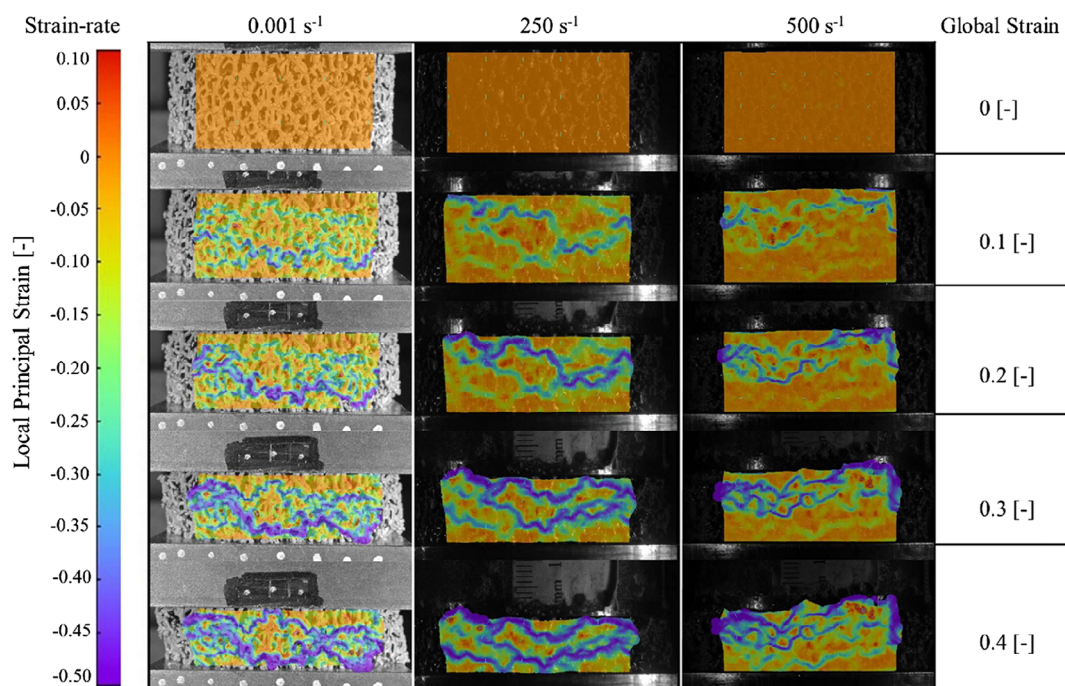


Figure 8. Local strain distribution at various global strain states for Ni/PU hybrid foams under quasistatic and dynamic loading.

still pronounced in the considered benchmarks. Therefore, the results of the IR camera confirm that there is no strain-rate-dependent material behavior under dynamic loads (Figure 5b). Considering the melting point $T_{m,Ni}$ of Ni with $1455\text{ }^{\circ}\text{C}$ leads to a low maximum homologous temperature T_{hom} of $T_{hom} = T/T_{m,Ni} = 0.052$. As a result, the temperature rise observed during the impact tests has a negligible effect on the mechanical material behavior.

3.3. Micromechanical Deformation Mechanism under Quasistatic and Dynamic Loading

The micromechanical deformation mechanism of Ni/PU hybrid foams under quasistatic and moderate dynamic loading was investigated using a high-speed camera and DIC. Figure 8 shows the local principal strain of three 50 mm diameter specimens under different strain rates at various global strain states. The first localized deformation band emerges after the PCS. It is visible at a global strain state of $\epsilon = 0.1$ under all considered strain rates. The deformation band extends over the entire cross-section and is mainly located in the middle of the specimen. This initial deformation band corresponds to the collapse of the first pore layer. Due to the inhomogeneous coating thickness, this pore layer is the weakest. With respect to the specimen geometry, a global strain state of $\epsilon = 0.1$ is equivalent to a displacement of about 2 mm. Considering a mean pore length of 1.3 mm, most of the global deformation is caused by the deformation of this pore layer.

The DIC images of all the considered specimens indicate a low-level strain distribution in the areas above and below the first deformation band. However, indications of further deformation bands are already emerging. For the quasistatic DIC image, there is one further deformation band developing, whereas under dynamic loading there are several further more or less completely pronounced deformation bands activated and distributed over the entire specimen. This suggests that during the PCS under dynamic loading, significant straining is occurring in multiple deformation bands giving a proof for the aforementioned change in the deformation mechanism under dynamic loading. It follows that the PCS is higher under dynamic loading than under quasistatic loading, which confirms the results from Figure 4a. At a global strain state of $\epsilon = 0.2$, which corresponds to a displacement of about two times the average pore size, the first deformation band is much more pronounced. One of the subsequent deformation bands is predominant for all considered specimens. This effect is further driven by microinertia effects due to local masses oscillating after the impact between the different pore layers.

In summary, more deformation bands are activated under dynamic loads at the moment of impact, resulting in an increased material resistance. However, these bands simply enlarge in the further progress of global strain. Therefore, the deformation mechanism of the dynamically formed deformation bands after the impact is similar to the quasistatic experiments. Therefore, the energy absorption capacity over the entire deformation range is not enhanced for the dynamic experiments.

4. Conclusion

The mechanical properties under quasistatic (10^{-3} s^{-1}) up to low-velocity impact (550 s^{-1}) strain rates of open-cell Ni/PU hybrid foams have been investigated. Quasistatic and drop-weight tests were conducted and recorded with a high-speed camera and an IR camera, on the one hand to gain a deeper insight in the micro-mechanical deformation mechanisms and on the other hand to evaluate the evolving specimen temperature during impact.

Regardless the specimen size, all specimens exhibit a 66% higher density-specific PCS under dynamic loads compared with quasistatic loads. However, the dynamically determined PCS shows no further strain-rate sensitivity in the observed strain-rate range under consideration. Although there is a pronounced strain-rate sensitivity for the PCS, there is no dependency of the energy absorption capacity from the strain rate for both specimen sizes.

An investigation of the temperature development during impact outlined that the evolving thermal energy leads to a low homologous temperature of the specimens. Thus, there is no significant influence on the mechanical behavior. A potential strain-rate sensitivity is not hidden behind a softening of the material.

The DIC analysis of the experiments under quasistatic and dynamic loading indicated a difference in the specific micromechanical deformation mechanism. The deformation bands are gradually activated under quasistatic loads, whereas several deformation bands are already activated after the PCS under dynamic loads leading combined with microinertia effects to a higher PCS under dynamic loads. However, neither the quantity nor the characteristics of the deformation bands change under progressing strain.

Acknowledgements

The authors gratefully acknowledge the ERASMUS+ program for financial support of Markus Felten.

Conflict of Interest

The authors declare no conflict of interest.

Keywords

drop-weight testing, hybrid metal foams, strain-rate effects, thermography

Received: December 30, 2019

Revised: March 12, 2020

Published online: May 26, 2020

-
- [1] J. Banhart, *Adv. Eng. Mater.* **2013**, *15*, 82.
 [2] J. Lázaro, E. Solórzano, M. A. Rodríguez-Pérez, *Adv. Eng. Mater.* **2017**, *19*, 1600496.
 [3] X. Wang, S. Xu, S. Zhou, W. Xu, M. Leary, P. Choong, M. Qian, M. Brandt, Y. M. Xie, *Biomaterials* **2016**, *83*, 127.
 [4] J. Marx, A. Rabiei, *Adv. Eng. Mater.* **2017**, *19*, 1600776.

- [5] A. Jung, Z. Chen, J. Schmauch, C. Motz, S. Diebels, *Acta Mater.* **2016**, 102, 38.
- [6] M. F. Ashby, A. Evans, N. A. Fleck, L. J. Gibson, J. W. Hutchinson, H. N. G. Wadley, *Metal Foams: A Design Guide*, Elsevier, Oxford, UK **2000**.
- [7] M. F. Ashby, R. F. M. Medalist, *Metall Mater. Trans. A* **1983**, 14, 1755.
- [8] J. Banhart, *Prog. Mater.* **2001**, 46, 559.
- [9] L. P. Lefebvre, J. Banhart, D. C. Dunand, *Adv. Eng. Mater.* **2008**, 10, 775.
- [10] A. Jung, L. A. A. Beex, S. Diebels, S. P. A. Bordas, *Mater. Des.* **2015**, 87, 36.
- [11] A. Jung, A. D. Pullen, W. G. Proud, *Composites A* **2016**, 85, 1.
- [12] A. Klavzar, M. Chiroli, A. Jung, B. Reck, *Proc. Eng.* **2015**, 103, 294.
- [13] G. W. Ma, Z. Q. Ye, *Int. J. Impact Eng.* **2007**, 34, 329.
- [14] H. Zhao, I. Elnasri, S. Abdennadher, *Int. J. Mech. Sci.* **2005**, 47, 757.
- [15] P. K. Pinnaji, P. Mahajan, N. Bourdet, C. Deck, R. Willinger, *Int. J. Impact Eng.* **2010**, 37, 274.
- [16] T. Sieber, U. Mühlich, T. Liedke, U. Ballaschk, H. Berek, C. G. Aneziris, D. Ehinger, S. Wolf, L. Krüger, *Steel Res. Int.* **2011**, 82, 1004.
- [17] I. N. Orbulov, K. Májlinger, *Mater. Des.* **2013**, 49, 1.
- [18] A. Jung, H. Natter, S. Diebels, E. Lach, R. Hempelmann, *Adv. Eng. Mater.* **2011**, 13, 23.
- [19] A. Jung, H. Natter, R. Hempelmann, S. Diebels, M. R. Koblishka, U. Hartmann, E. Lach, *ECS Trans.* **2010**, 25, 165.
- [20] A. Jung, S. Diebels, *Adv. Eng. Mater.* **2016**, 18, 532.
- [21] R. Rybár, M. Beer, D. Kudelas, B. Pandula, *Metalurgija* **2016**, 55, 489.
- [22] Y. J. Li, Y. L. Ren, Z. D. Li, F. S. Han, *Mater. Sci. Forum* **2014**, 783–786, 1509.
- [23] G. C. Koltsakis, D. K. Katsaounis, Z. C. Samaras, D. Naumann, S. Saberi, A. Böhm, *Filtration and Regeneration Performance of a Catalyzed Metal Foam Particulate Filter (No. 2006-01-1524)*, SAE Technical Papers **2006**.
- [24] F. García-Moreno, *Materials* **2016**, 2, 85.
- [25] V. S. Deshpande, N. A. Fleck, *Int. J. Impact Eng.* **2000**, 24, 277.
- [26] L. J. Gibson, M. F. Ashby, *Cellular Solids*, Cambridge University Press, Cambridge **1997**.
- [27] X. Y. Su, T. X. Yu, S. R. Reid, *Int. J. Impact Eng.* **1995**, 16, 673.
- [28] X. Y. Su, T. X. Yu, S. R. Reid, *Int. J. Impact Eng.* **1995**, 16, 651.
- [29] C. R. Calladine, R. W. English, *Int. J. Mech. Sci.* **1984**, 26, 689.
- [30] M. Altenajji, Z. W. Guan, W. Cantwell, Y. Y. Zhao, *Appl. Mech. Mater.* **2014**, 564, 449.
- [31] A. Jung, E. Lach, S. Diebels, *Int. J. Impact Eng.* **2014**, 64, 30.
- [32] T. Fiedler, M. Taherishargh, L. Krstulović-Opara, M. Vesenjak, *Mater. Sci. Eng. A* **2015**, 626, 296.
- [33] S. Xu, D. Ruan, G. Lu, *Int. J. Impact Eng.* **2014**, 74, 120.
- [34] A. S. M. Ashab, D. Ruan, G. Lu, Y. C. Wong, *Mater. Des.* **2016**, 97, 183.
- [35] D. Zhang, Q. Fei, P. Zhang, *Compos. Struct.* **2017**, 168, 633.
- [36] D. Zhang, D. Jiang, Q. Fei, S. Wu, *Finite Elem. Anal. Des.* **2016**, 117–118, 21.
- [37] X. Pang, H. Du, *Composites B* **2017**, 112, 265.
- [38] S. Hong, J. Pan, T. Tyan, P. Prasad, *Int. J. Plast.* **2008**, 24, 89.
- [39] V. Crupi, G. Epasto, E. Guglielmino, *J. Sandwich Struct. Mater.* **2011**, 13, 409.
- [40] S. Ramachandra, *Scr. Mater.* **2003**, 49, 741.
- [41] G. Castro, S. R. Nutt, X. Wenchen, *Mater. Sci. Eng. A* **2013**, 578, 222.
- [42] M. A. Hazizan, W. J. Cantwell, *Composites B* **2003**, 34, 679.
- [43] M. A. Islam, M. A. Kader, A. D. Brown, P. J. Hazell, J. P. Escobedo, M. Saadatfar, *Charact. Miner. Met. Mater.* **2017**, 2017, 225.
- [44] Y. Hangai, N. Kubota, T. Utsunomiya, H. Kawashima, O. Kuwazuru, N. Yoshikawa, *Mater. Sci. Eng. A* **2015**, 639, 597.
- [45] J. U. Cho, S. J. Hong, S. K. Lee, C. Cho, *Mater. Sci. Eng. A* **2012**, 539, 250.
- [46] M. Altenajji, Z. W. Guan, W. J. Cantwell, Y. Zhao, G. K. Schleyer, *Mater. Des.* **2014**, 59, 296.
- [47] S. Cheng, B. Xiao, X. Zhao, Y. Xin, H. Li, *J. Mater. Res.* **2017**, 32, 2258.
- [48] R. A. W. Mines, S. Tsopanos, Y. Shen, R. Hasan, S. T. McKown, *Int. J. Impact Eng.* **2013**, 60, 120.
- [49] A. Jung, K. Al Majthoub, C. Jochum, S. M. Kirsch, F. Welsch, S. Seelecke, S. Diebels, *J. Mech. Phys. Solids.* **2019**, 130, 165.
- [50] R. Juntikka, S. Hallström, *Int. J. Impact Eng.* **2004**, 30, 541.
- [51] K. R. Mangipudi, S. W. van Buuren, P. R. Onck, *Int. J. Solids Struct.* **2010**, 47, 2081.
- [52] M. Kolluri, S. Karthikeyan, U. Ramamurty, *Metall. Mater. Trans. A* **2007**, 38, 2006.
- [53] A. Jung, M. R. Koblishka, E. Lach, S. Diebels, H. Natter, *Int. J. Mater. Sci.* **2012**, 2, 97.